



Effect of carbon quantum dots and Zn²⁺ ion on perovskite solar cells

Hadeer Hussien¹, Zekry Ghatass¹, M. S. Hassan², Moataz Soliman³, and Shaker Ebrahim^{3,*} 

¹Department of Environmental Studies, Institute of Graduate Studies and Research, Alexandria University, P.O. Box 832, Alexandria, Egypt

²Department of Physics, Faculty of Science, Alexandria University, P.O. Box 21511, Alexandria, Egypt

³Department of Materials Science, Institute of Graduate Studies and Research, Alexandria University, P.O. Box 832, Alexandria, Egypt

Received: 21 February 2023

Accepted: 26 June 2023

Published online:

27 July 2023

© The Author(s) 2023

ABSTRACT

Perovskite solar cells (PSCs) have a great attention due to their remarkable performance and a high-quality perovskite film is necessary to achieve high power conversion efficiency (PCE). The effect of carbon quantum dots (CQDs) and Zn²⁺ ions on perovskite layer of methyl ammonium lead iodide (MAPbI₃) was investigated. The optical, structural, and morphological properties of perovskite films with different Zn²⁺ ratios and CQDs contents were investigated. It was observed that 1% ZnCl₂ /0.05 mg/mL CQDs perovskite film composed of uniform grains distribution, complete surface coverage with negligible pinholes, and a larger grain size of 1.8 μm. In addition, it was found that increasing CQDs contents to 0.1 and 0.25 mg/mL enlarged the grain size to ~ 4.2 μm. Moreover, the incorporation of CQDs enhanced crystallinity and grain size. Consequently, these improvements were reflected on the solar cell performance and the efficiency of PSCs with additive of 1% ZnCl₂-0.05 mg/mL CQDs was improved from 4.21 to 8.08%.

1 Introduction

Perovskite solar cells (PSCs) have recently flourished as a good candidate for photovoltaic technology due to their low cost with a considerable power conversion efficiency and their superior optoelectronic properties such as high absorption coefficient and low direct bandgap. Organic-inorganic halide perovskite is commonly applied in PSCs where a

remarkable growth in PCE from 3.18 to 25.7% in a short time was achieved. However, the low stability and high sensitivity for humidity and oxygen are the main problems facing PSCs [1–3]. In addition, the perovskite film deposited from solution suffers from the presence of different surface defects such as grain boundaries, uncoordinated Pb²⁺ and anti-site PbI⁻ [4]. These defects can form localized trap states and act as recombination centers for the charge carriers.

Address correspondence to E-mail: shaker.ebrahim@alexu.edu.eg

Therefore, the passivation of these defects results in an enhancement of PSCs performance. There are several passivation routes employed to passivate the surface trap states of the perovskite active layer such as anion replacement, metal cation replacement, and small molecule additives [5, 6]. Pb^{2+} ions replacement by other divalent cations, like lanthanides, alkali metals, and transition metals was studied [7–9]. Zinc metal has high abundance in the Earth's crust and is a non-toxic metal. In addition, it is a medium-sized transition metal with an atomic radius of 74.0 pm and this is smaller than the atomic radius of Pb^{2+} (119 pm) [10]. Zn^{2+} has a suitable valence state and resistant to reduction and oxidation processes [11]. Zn^{2+} has higher chemical activity than Pb^{2+} and reinforces the ability to coordinate with CH_3NH_3^+ [12]. Therefore, Zn^{2+} is supposed to have a good influence on perovskite film morphology. Goldschmidt tolerance factor (t) is used to estimate the type and stability of the crystal structure [13]. This factor for organometal halide perovskite is ranged between $0.813 < t < 1.1$ and is expressed by the following equation [14]:

$$t = \frac{r_A + r_X}{\sqrt{2}(r_B + r_X)} \quad (1)$$

where r_A , r_B , and r_X are the radii of A cation, B cation, and X anion, respectively. On the other hand, the tolerance factor of $\text{CH}_3\text{NH}_3\text{ZnI}_3$ is 1.05 [15]. This means that Zn^{2+} has the capacity to form $\text{CH}_3\text{NH}_3\text{-PbI}_{(1-x)}\text{ZnCl}_x$ perovskite structure. In addition, the undercoordinated Pb^{2+} cations can be passivated by forming coordinated bond with electron-rich Lewis bases to eliminate the positive charge at the perovskite grain surface [16].

The incorporation of carbon-based nanostructures was added to the perovskite precursor to improve film quality, surface coverage, obtain large grain size, and decrease the grain boundaries. The incorporation of carbon-based nanostructures is also a powerful solution to increase the stability of PSCs [17–19]. Among the various carbon-based nanostructures, CQDs possess attractive properties of high stability, good conductivity, low toxicity, simple synthetic routes as well as comparable optical properties to QDs [20–22]. Guo et al. detected the interaction between CQDs and MAPbI_3 by infrared spectra and they noted that the vibration peak of C=O in CQDs was shifted from 1713 to 1705 cm^{-1} . This shift

indicates a strong interaction between CQDs and MAPbI_3 [23]. Ma et al. introduced three different concentrations of CQDs (0.1, 0.15, and 0.2 mg/mL) and reported an enhancement in photoluminescence intensity, carrier lifetime, and PCE from 15.67 to 18.24%. They found that PSC with 0.15 wt% CQDs remains 73.4% of its initial PCE after 48 h in the dark at ambient temperature and 80% relative humidity [24].

Herein, the incorporation of CQDs as a passivator for the grain boundaries along with Zn^{2+} ions to passivate the uncoordinated lead ions and partially substitute Pb^{2+} ions to form a stable perovskite structure are carried out. The effect of three ratios of CQDs (0.02, 0.05, 0.10 and 0.25) combined with the doping ratio of 1% ZnCl_2 on the optical, structural and morphological properties of perovskite layer are investigated. The conventional structure of PSCs composed of ITO/ TiO_2 /active layer/spirito-OMeTAD /Carbon is fabricated and evaluated.

2 Experimental work

2.1 Materials

Lead iodide, methylammonium iodide (MAI), lithium bis-(trifluoromethanesulfonyl)imide (Li-TFSI), 4-tert-butyl pyridine (tBP), dimethylsulfoxide (DMSO) and chlorobenzene were obtained from Sigma-Aldrich. Spiro-OMeTAD (2,20,7,7'-tetrakis (N,N-di-p-methoxyphenylamine)-9,9'-spiro-bifluorene) was purchased from Ossila. Zinc chloride was received from Merck. N, N dimethylformamide (DMF), sodium hydroxide 98% was purchased from Fisher Scientific. Titanium (IV) isopropoxide (98%) and acetylacetone were got from Across Organics and Alpha Chemika, India, respectively. Fluorine-doped tin oxide (FTO) with $15 \text{ Ohm}/\square$ was bought from Nanocs Company, USA.

2.2 Synthesis of CQDs

CQDs were synthesized by aldol condensation reaction. Specifically, 8 g of NaOH was dissolved in 40 mL of acetone under vigorous stirring for 1 h, and this mixture was kept at room temperature for 120 h. The formed solid mixture was neutralized with 1 M HCl, separated centrifugally at 4000 rpm for 20 min,

and washed with deionized water several times. Then the final produced CQDs were dried at 80 °C for 24 h [25].

2.3 TiO₂ and carbon paste preparation

To prepare TiO₂ precursor solution, 0.6 mL of titanium (IV) isopropoxide was added to 0.4 mL of acetylacetone and mixed by stirring for 30 min. Then 9 mL of ethanol was added to this mixture with a continuous stirring for 30 min [26]. The carbon paste was prepared according to previously reported work [27]. A mixture with 30 wt% carbon black and graphite powder with ratio of 1:3 in chlorobenzene was stirred for 30 min. After that, 10 wt% of ethyl cellulose dissolved in chlorobenzene was added and stirred for 1.0 h.

2.4 Perovskite precursors preparation

Perovskite precursors with different compositions were prepared in the nitrogen-filled glove box (Innovation Technology Company). The pristine CH₃NH₃PbI₃ precursor was prepared by dissolving 159 mg MAI and 461 mg PbI₂ in 1.0 mL DMF:DMSO (3:7 v/v) with a continuous stirring overnight at 60 °C. A stock solution of CQDs (5.0 mg/mL) suspended in DMF was prepared. The second doped perovskite precursor with ZnCl₂ of different ratios was synthesized as (MAI) (PbI₂)_{1-x} (ZnCl₂)_x where ($x = 1, 3, \text{ and } 5\%$) [28]. Finally, the third precursor was CQDs of 0.02, 0.05, 0.1, 0.25 (mg/mL) combined with 1% ZnCl₂ doped perovskite.

2.5 Fabrication of perovskite solar cells

Perovskite solar cells were assembled using a planer conventional structure of FTO/c-TiO₂/active perovskite layer/spiro OMeTAD/carbon electrode. FTO substrates were etched with Zn powder and 2.0 M HCl and then sequentially cleaned with Helmanix, deionized water, acetone and isopropanol. Two layers of compact titanium oxide (c-TiO₂) were spun, where 60 μL of TiO₂ solution was deposited onto the cleaned FTO substrate at 2000 rpm for 30 s and dried at 100 °C for 10 min. The obtained c-TiO₂ films were sintered at 450 °C for 30 min [26]. Inside the nitrogen-filled glove box, the perovskite layers were spun onto FTO/c-TiO₂ through two steps process at 1000 and 4000 rpm for 10 and 30 s, respectively.

Chlorobenzene (100 μL) was quickly and continuously dropped on the perovskite layers for 10 s prior to the end of the second step. The obtained FTO/c-TiO₂/perovskite layers were annealed at 100 °C for 20 min [29, 30]. A thin layer of spiro-OMeTAD (70 mg/mL in chlorobenzene) doped with 18 μL lithium bis (trifluoromethanesulfonyl) imide (Li-TFSI) solution (520 mg Li-TFSI in 1 mL acetonitrile), and 33 μL TBP (4-tert-butylpyridine) was coated at 2000 rpm for 20 s and oxidized in air for 60 min. Finally, the carbon counter electrode was fabricated by using the doctor-blade technique and dried at 100 °C for 20 min [27].

2.6 Characterization techniques and measurements

The absorption spectra of perovskite films were investigated using UV-vis spectrophotometer (Evolution 600 double beams scanning spectrophotometer, Thermo Scientific, USA). Fourier transform infrared (FTIR) spectra of the CQDs were obtained using (Spectrum BX 11 spectrometer FTIR LX 18-5255 Perkin Elmer). The photoluminescence spectra were recorded for the different perovskite layers coated on glass substrate by fluorescence spectrophotometer (Perkin Elmer-LS 55). The contact angle of a drop of water and perovskite surface was measured using a contact angle goniometer (Ramé-hart CA instrument, model 190-F2). X-ray diffraction (XRD) patterns were obtained using XRD, D2 PHASER, Bruker and the X-ray source was Cu target generated at 30 kV and 10 mA. The morphology of perovskite films was investigated by scanning electron microscope (SEM “JEOL-IT200”, Japan) at an acceleration voltage of 25 kV. The morphology of CQDs was confirmed by field emission transmission electron microscope (FE-TEM) (JEOL JEM -2100 F, Japan). Atomic force microscope (AFM) (Shimadzu, SPM 9700, USA) was used to image the topography in the tapping mode for the perovskite layers deposited on FTO/c-TiO₂ film. The photovoltaic performance was evaluated in air under simulated illumination generated by Xenon lamp at intensity of 680 W/cm², which was calibrated by monocrystalline Si standard solar cell. Current density-voltage characteristic curves under darkness and illumination were obtained by using Autolab Potentiostat/Galvanostat PGSTAT 204 with a scan rate of 100 mV/s in forward bias.

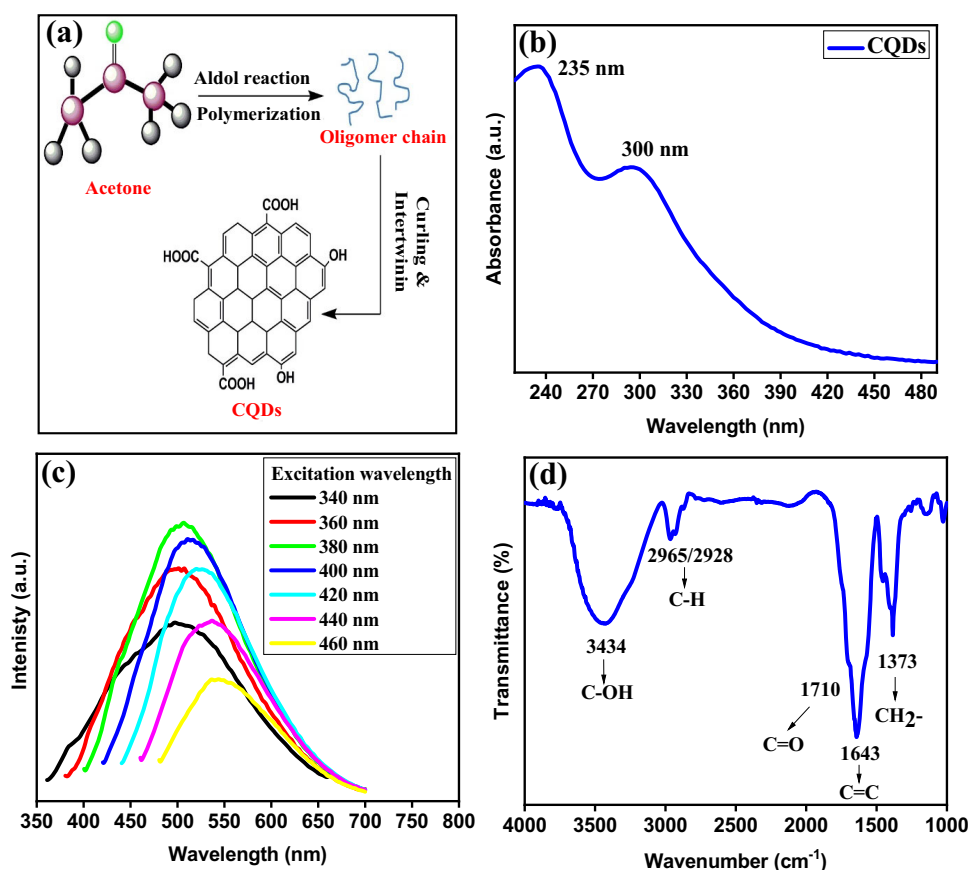
3 Results and discussion

The formation of CQDs is proposed via the synthesis of aromatic clusters by aldol condensation from acetone assisted by NaOH as illustrated in Fig. 1a. The aldol reaction of acetone in presence of alkaline medium can occur and result in the formation of an unsaturated ketone. Afterward, the polymerization process of this unsaturated ketone forms oligomers with extended carbon chains which curl and intertwine to produce CQDs. The absorption of the as-prepared CQDs depicted in Fig. 1b has two peaks at around 235 and 300 nm attributed to π - π^* transition of C=C (carbonic core) and n - π^* electronic transition, respectively [31, 32]. To examine the fluorescence properties of CQDs, PL spectra of CQDs dissolved in DMF at different excitation wavelengths (340–460 nm) are recorded and illustrated in Fig. 1c. It is noticed that the fluorescence intensity is decreased, and the emission peak is red shifted from 500 to 550 nm as λ_{ex} is increased from 340 to 460 nm, respectively. This reveals a wavelength dependence photoluminescence behavior of CQDs. The tunable

emission wavelength and intensity of CQDs originate from the broad size distribution, surface defects and surface states. It is noted that the fluorescence emission results from the radiative recombination of electron-hole pairs and consequently the decline in fluorescence intensity confirms the presence of surface trap states. The tunable of CQDs size affects the nature, content of sp^2 hybridized sites and value of the band gap [33–35]. To study the surface structure and composition of CQDs, FTIR analysis is carried out as represented in Fig. 1d. The stretching vibration at 3434 cm^{-1} is assigned to OH group. The CH and CH_2 stretching vibrations from the residues of methyl groups of acetone are located at 2965 and 2928 cm^{-1} , respectively. In addition, the vibrational bands at 1710 and 1643 cm^{-1} are attributed to C=O and C=C, respectively [25, 36].

FE-TEM investigation is carried out to obtain the structure and morphology of CQDs. TEM image illustrates the homogenous and well dispersed spherical CQDs with a diameter ranged between 5 and 9 nm as shown in Fig. 2a. The high resolution TEM image of a single crystal displayed in the inset

Fig. 1 Schematic illustration of CQDs preparation via aldol condensation (a), Absorbance spectrum of CQDs dissolved in DMF (b), PL spectra of CQDs dissolved in DMF at different excitation wavelengths (c) and FTIR spectrum of CQDs (d)



of Fig. 2a indicates the crystalline nature of CQDs with a lattice space of 0.24 nm and this is compatible with (002) of graphite structure [37, 38]. Selected area electron diffraction (SAED) is a technique applied alongside TEM to determine the crystallinity and crystal nature of CQDs. The single-crystalline diffractogram depicts a regular pattern of bright spots. If there are more contributing crystallites in polycrystalline material, the diffraction image results from a superposition of individual single crystals. This superposition contains diffraction spots of the crystallographic planes in all orientations. In case of SAED of CQDs taken from one or a few single crystals, the diffractogram depicts a regular pattern of bright spots as represented in Fig. 2b [39].

The crystalline structure of the synthesized CQDs is identified via XRD analysis. As depicted in Fig. 2c, CQDs exhibit XRD patterns with broad peaks on a huge characteristic hump [40]. CQDs have a strong peak at 29.27°, which is ascribed to (002) (JCPDS, Card No. 75-1621) [41]. In addition, there is a small peak centered at 55.08° assigned to (004). Both (002) and (004) represent the characteristic planes of graphitic carbon in the synthesized CQDs [41, 42]. However, sharp, and faint peaks located at 17.05° and

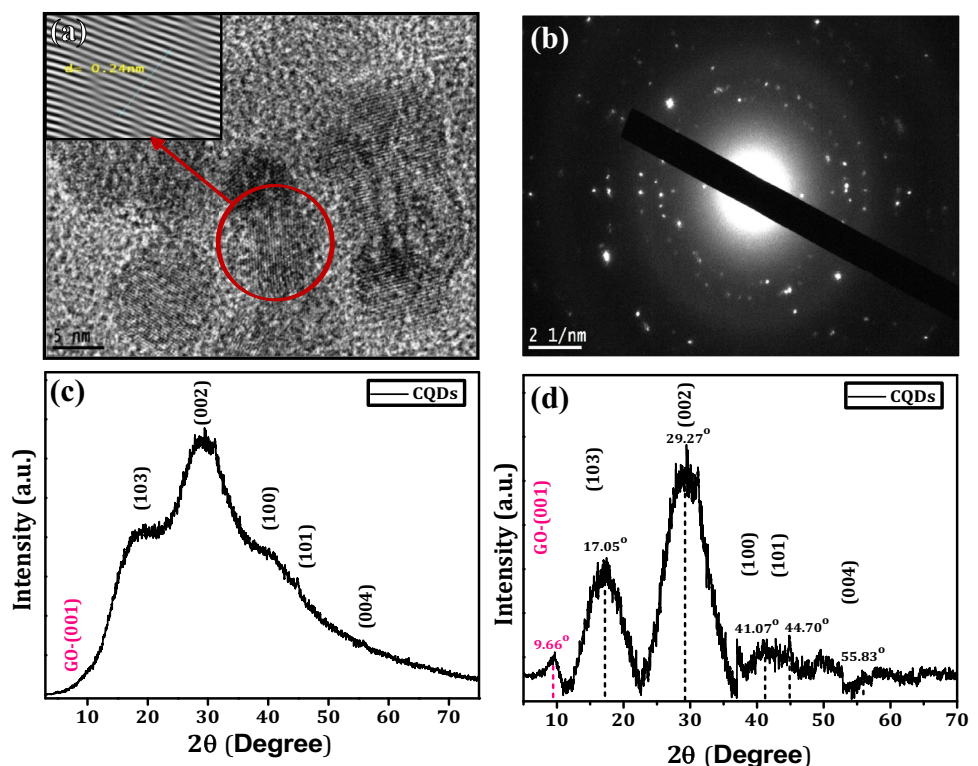
44.07° are attributed to (103) and (101) planes, respectively. This confirms the co-existence of both graphitic and amorphous carbon nature in the synthesized CQDs [40]. It is found that the percentage of crystallinity or the percent relative crystallinity (X_c) is 61% [43].

By applying Bragg’s Law, the interlayer spacing (d -spacing, d_{hkl}) of the characteristic peak (002) is 0.31 nm which is lower than the graphitic interlayer spacing (0.33 nm) [42]. The lower value of d -spacing indicates the small crystalline nature of the synthesized CQDs. It is noted that the broadening of (002) plane suggests the ultrafine crystallite size of CQDs. Thus, to estimate the average crystallite size (D) of the CQDs, Debye-Scherrer’s equation is applied to the diffraction peaks of the CQDs (Eq. 2) [44] :

$$D = \frac{K\lambda}{\beta \cos \theta} \tag{2}$$

where K is a shape factor of 0.89, λ is the wavelength of X-rays, β is full width at half maximum (FWHM), and θ is Bragg’s diffraction angle [45]. The baseline correction and Gaussian fitting are applied to XRD patterns [see Fig. 2d] to estimate the FWHM and D values as listed in Table 1. The mean crystallite size

Fig. 2 FE-TEM image with d -space (inset) (a), SAED of CQDs (b), and XRD patterns and baseline correction of the XRD patterns of CQDs (c,d)



of the CQDs of 1.17 nm corresponds to the most intense peak (002). Moreover, XRD patterns demonstrate that the CQDs contain graphene oxide (GO) with a peak located at 9.66° for (001). The crystallite size and the d -spacing of the GO are 1.82 and 0.92 nm, respectively [46]. The high value of d -spacing for GO is assigned to the intercalation of water molecules, oxygen-functional groups, and other structural defects between graphitic layers [47, 48].

XRD patterns for doped perovskite films with different ratios of ZnCl_2 are displayed in Fig. 3a. The peaks of (110), (220), and (310) planes are located at 14.13° , 28.45° , and 31.82° , respectively. The crystalline structure of perovskite films is a tetragonal structure and agrees with the previous work [49]. It is noted that the diffraction peak of (110) plane is shifted toward lower angles with increasing doping level of Zn content due to the substitution or incorporation of Zn ions in the perovskite lattice as shown in Fig. 3c [50]. The intensity of (110) and (220) planes is enlarged as ZnCl_2 concentration increases and FWHM of (110) plane becomes smaller, and this indicates an enhancement in the crystallinity of ZnCl_2 doped perovskite films. The enhancement in the crystallinity of ZnCl_2 doped perovskite films can be also attributed to the strong coordination interaction between Zn^{2+} and CH_3NH_3^+ . Zn^{2+} is a stronger Lewis acid than Pb^{2+} and this influences the crystallization growth during the annealing process [51]. However, PbI_2 degradation phase of (001) plane and located at 12.7° appears at 3 and 5% of Zn^{2+} is attributed to excess ZnCl_2 concentration and this decomposes the perovskite structure [49].

XRD patterns of 1% $\text{ZnCl}_2/\text{CQDs}$ based perovskite films with different CQDs contents are depicted in Fig. 3b. It is observed that the crystallinity of CQDs based perovskite films is enhanced and attained the optimal at 0.05 mg/mL with a reduction of impurity and degradation peak of PbI_2 . It is found that the

crystalline peaks of the perovskite films are attributed to the tetragonal structure. The absence of extra peaks in XRD pattern of perovskite films with addition of CQDs indicates that the CQDs do not affect the perovskite crystal structure. This is confirmed by the fixing of the angle position of (110) plane shown in Fig. 3d upon the incorporation of CQDs [23]. CQDs addition improves crystallinity of $\text{ZnCl}_2/\text{CQDs}$ based perovskite films due to the interaction between the CQDs surface functional groups and perovskite. Therefore, CQDs are adsorbed at the grain boundaries and restrict the evaporation of the solvent during film formation. This delays perovskite growth and improves the crystallization process [52]. Generally, the incorporation of CQDs along with 1% ZnCl_2 with a small amount (less than 0.05 mg/mL) can enhance the crystallinity of the perovskite film.

The absorption spectra of MAI $(\text{PbI}_2)_{1-x}(\text{ZnCl}_2)_x$ perovskite films with $x = 0, 1, 3$, and 5% have onset peaks around 775 nm as displayed in Fig. 3e. It is noticed that the absorbance of 1% ZnCl_2 doped film is increased due to the improvement of crystallinity of the perovskite films. However, the absorbance of MAI $(\text{PbI}_2)_{1-x}(\text{ZnCl}_2)_x$ perovskite films with 3 and 5% Zn^{2+} contents is reduced. This reduction results from the poor quality of the prepared films as confirmed by XRD and SEM [28]. The optical bandgap of the as-prepared pristine and 1% ZnCl_2 doped perovskite is determined using Tauc plots as depicted in the inset of Fig. 3e. The bandgap is slightly increased from 1.576 eV for the pristine film to 1.586 eV for 1% ZnCl_2 doped film [53]. Consequently, this small increment in the bandgap can be attributed to the participation of the more electronegativity of halogen chloride ions (the electron binding energies increase as $\text{Cl}^- > \text{Br}^- > \text{I}^-$) [54]. Figure 3f presents the absorbance spectra of 1% ZnCl_2 along with 0.02, 0.05, 0.1, and 0.25 mg/mL CQDs perovskite films. The spectra exhibit higher absorbances than 1% ZnCl_2 and

Table 1 Crystallographic parameters from XRD patterns of CQDs

	No.	hkl	$2\theta_{\text{XRD}} [^\circ]$	$2\theta_{\text{JCPDS}} [^\circ]$	$d_{\text{hkl}} (\text{XRD}) [\text{nm}]$	FWHM [Radian]	$D [\text{nm}]$
CQDs	1	(103)	17.05	8.53	0.5199	0.1069	1.31
	2	(002)	29.27	14.63	0.3051	0.1227	1.17
	3	(100)	41.07	20.54	0.2198	0.1289	1.15
	4	(101)	44.70	22.35	0.2027	0.0701	2.14
	5	(004)	55.83	27.92	0.1647	0.1082	1.45
$D_{\text{Average}} = 1.45 \pm 0.36 \text{ nm}$							
GO	1	(001)	9.66	4.83	0.9156	0.0763	1.82

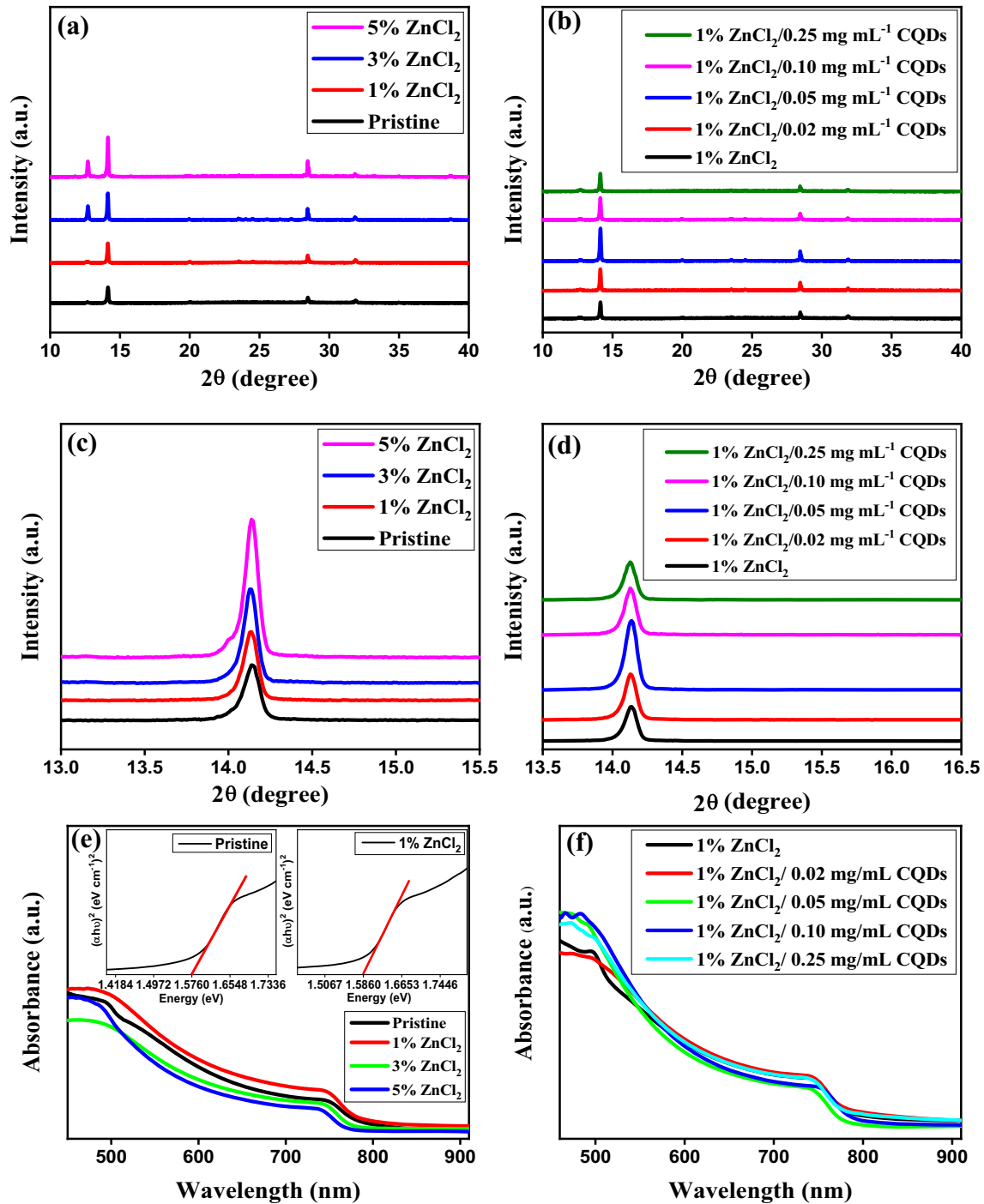


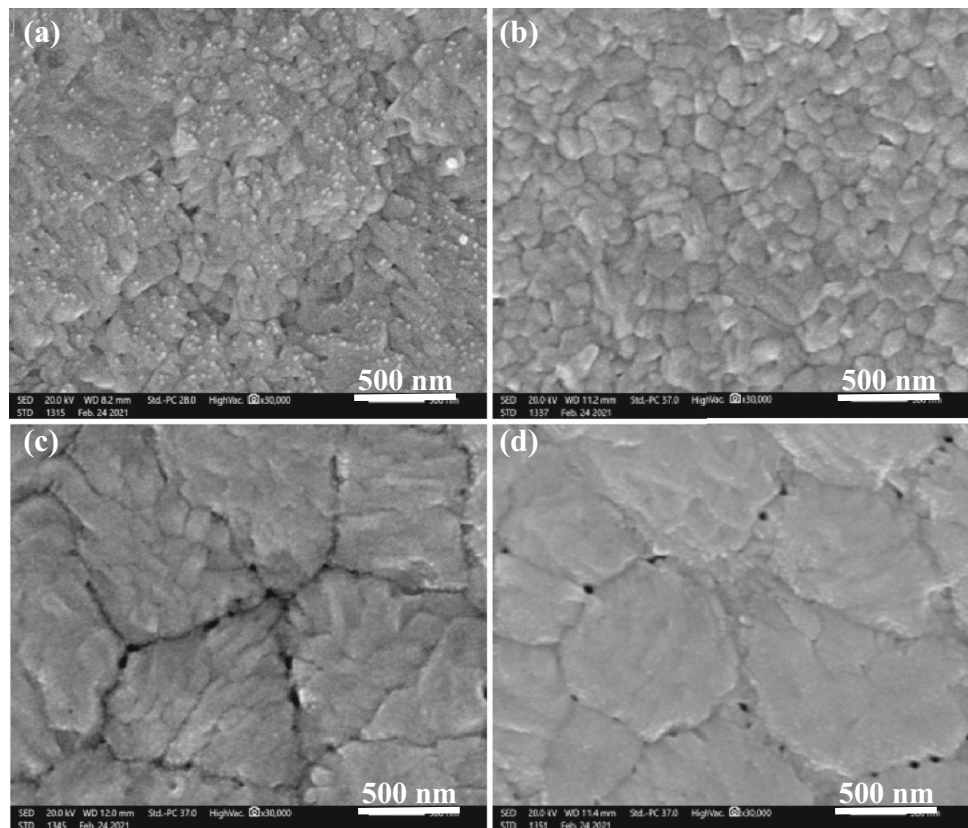
Fig. 3 XRD patterns of perovskite films with different ZnCl₂ contents (a), 1% ZnCl₂/CQDs based perovskite films with different CQDs contents (b), Enlargement of the peak representing (110) plane for both Zn and CQDs additives, respectively (c and d), UV-vis spectra of

MAI(PbI₂)_{1-x}(ZnCl₂)_x, x= 0, 1, 3, and 5% and Tauc plots of pristine and 1% ZnCl₂ films (inset) (e), and 1% ZnCl₂ incorporated with different CQDs concentrations perovskite films (f)

pristine films within the region from 450 to 550 nm. The spectra verify the valuable impact of introducing CQDs with ZnCl₂ on perovskite film quality.

Figure 4a–d depicts SEM photographs to investigate the effect of ZnCl₂ on the nucleation and crystal growth process of perovskite film with different

Fig. 4 SEM surface images of MAI(PbI₂)_{1-x}(ZnCl₂)_x, $x=0, 1, 3,$ and 5% (a–d), respectively



ratios of zinc chloride (1, 3, and 5%). It is observed that pristine film exhibits non-uniform grains with an average grain size of 197 nm and few pinholes. The grain size of 1% ZnCl₂ perovskite has enlarged to be about ~ 340 nm and this film is uniform, dense, and compact. In addition, for 3 and 5% ZnCl₂ perovskite films, the grain size is significantly increased to ~ 1.5 μm , and the pinholes and cracks are observed at the grain boundaries. This affects the film quality and generates leakage paths and it is expected to reduce the photovoltaic performance [55]. Jin. et al. compared the effect of ZnCl₂ and ZnI₂ on the morphology of perovskite to determine whether the crystal grain size is mainly associated with Zn²⁺ or Cl⁻. They concluded that the perovskite film prepared with ZnI₂ has a grain size similar to ZnCl₂ revealing the crucial impact of Zn on the crystal growth process [28]. It is expected that during the perovskite crystal growth, the small portion of Zn²⁺ ions substitute Pb²⁺ ions location in the perovskite framework to change the crystallization process. The higher chemical interaction between Zn²⁺ and anions, along with a strong coordination function

with organic groups, produces doped perovskite film with a higher grain size [51].

In addition, SEM images of CQDs with different contents incorporated into 1% ZnCl₂ doped perovskite films are illustrated in Fig. 5a–d. The obtained 1% ZnCl₂ /0.05 mg/mL CQDs perovskite film has uniform grains, high surface coverage with negligible pinholes, and large grain size of ~ 1.8 μm . For 0.1 and 0.25 mg/mL of CQDs, the grain size of 1% ZnCl₂ doped perovskite films is enlarged to ~ 4.2 μm . However, the high content of CQDs is synchronized with the appearance of pinholes inside and between the grains. Guo et al. proposed a decrease in the grain size with increasing CQDs content [23]. This is contradictory to our results. CQDs incorporated with ZnCl₂ lead enlarged to the grain size and this reveals a good impact of CQDs incorporation with ZnCl₂ for getting a compact perovskite film with negligible defects.

AFM analysis is carried out to study the effect of incorporation of ZnCl₂ and CQDs on topography of perovskite films. Figure 6a–c displays AFM images of pristine, 1% ZnCl₂, and 1% ZnCl₂-0.05 mg/mL CQDs based perovskite films, respectively. The bright

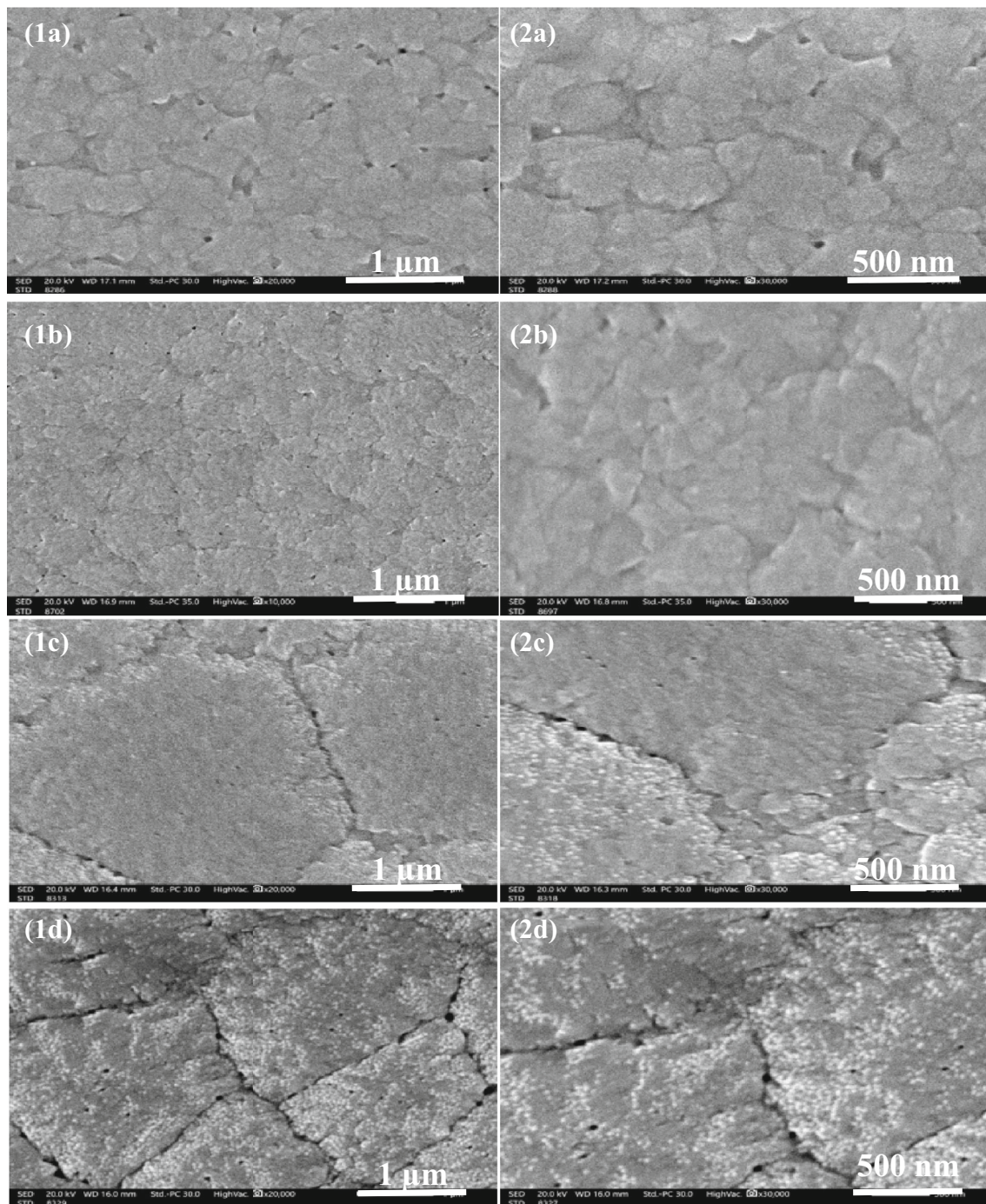


Fig. 5 SEM images of 1% ZnCl_2 perovskite film surface with different CQDs concentrations 0.02, 0.05, 0.1 and 0.25 mg/mL (a–d), respectively

regions represent the highest peaks, while the dark regions refer to the deep valleys and pinholes [56]. The arithmetical mean roughness (R_a) values are 17.2, 22.9, and 19.4 nm for pristine, doped 1% ZnCl_2 , and 1% $\text{ZnCl}_2/0.05 \text{ mg mL}^{-1}$ based CQDs perovskite films, respectively. After adding ZnCl_2 (1%), the

roughness of the perovskite film has slightly increased and negligible grooves are observed compared with the pristine film. On the other hand, the roughness of 1% $\text{ZnCl}_2/0.05 \text{ mg/mL}$ CQDs based perovskite film is slightly reduced again.

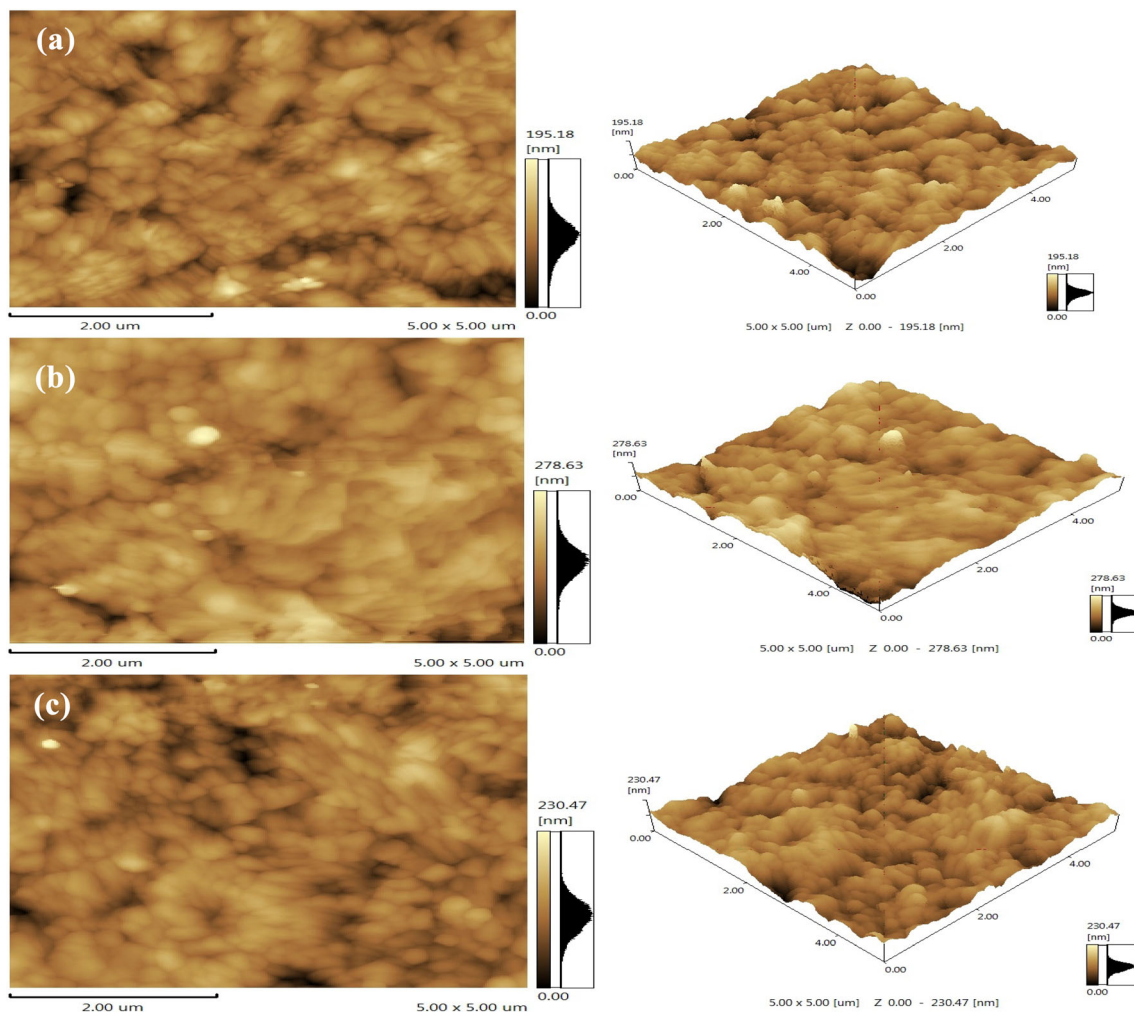


Fig. 6 AFM images of perovskite films; pristine (a), 1% ZnCl_2 (b), and 1% $\text{ZnCl}_2/0.05 \text{ mg mL}^{-1}$ CQDs (c)

Current density versus voltage (J–V) curves are measured to investigate the effect of ZnCl_2 and CQDs on the PSCs performance. Figure 7a presents J–V curves of pristine FTO/c-TiO₂/perovskite/carbon

electrode, FTO/c-TiO₂/1% ZnCl_2 doped perovskite/carbon electrode, and FTO/c-TiO₂/1% $\text{ZnCl}_2/0.05 \text{ mg mL}^{-1}$ CQDs perovskite/carbon electrode under illumination power of 680 W/m^2 .

Fig. 7 J–V curves of pristine FTO/c-TiO₂/perovskite/carbon electrode, FTO/c-TiO₂/1% ZnCl_2 doped perovskite/carbon electrode, and FTO/c-TiO₂/1% $\text{ZnCl}_2/0.05 \text{ mg mL}^{-1}$ CQDs perovskite/carbon electrode under forward scan mode and illumination power of 680 W/m^2 (a), Semi log dark J–V curves (b)

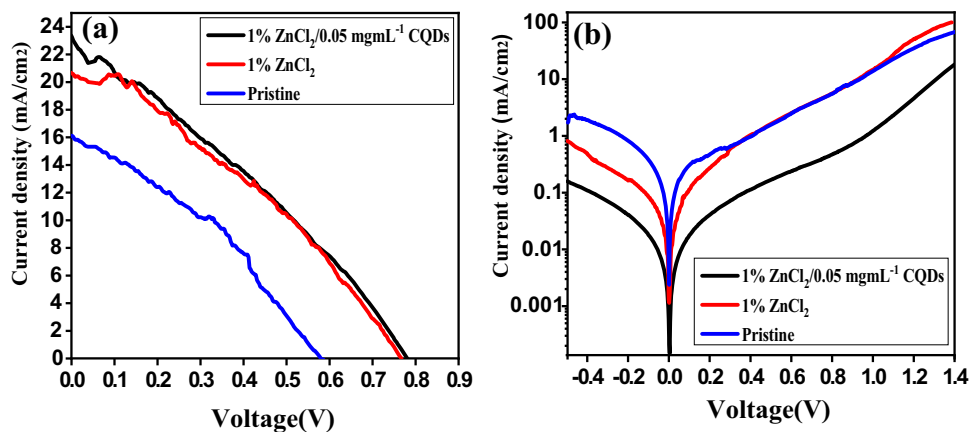


Table 2 The photovoltaic characteristics of PSCs with different additives

Device	J_{sc} (mA/cm ²)	V_{oc} (V)	FF (%)	PCE (%)
Pristine	16	0.56	32	4.21
1% ZnCl ₂	20.5	0.75	33.7	7.61
1% ZnCl ₂ /0.05CQDs	23.5	0.78	30	8.08

Table 2 summaries the photovoltaic parameters for the perovskite solar cells with different additives. By introducing 1% ZnCl₂, V_{oc} and J_{sc} are improved compared to the pristine perovskite solar cell. It is found that V_{oc} and J_{sc} for pristine PSCs are 0.56 V and 16 mA/cm² while for 1% ZnCl₂/0.05 CQDs PSCs are 0.78 V and 23.5 mA/cm², respectively. On the other hand, FF value is slightly decreased. This reduction could be caused by the insufficiency of carrier extraction at c-TiO₂ layer and carbon counter electrode interfaces. The shunt (R_S) and series (R_{SH}) resistances have impact on the FF. The lower value of R_{SH} results in parasitic current pathways in parallel to the ideal diode and the high value of R_S shifts the working point due to a parasitic voltage drop over the series resistance [57]. The series resistance losses occur due to the recombination process at carbon electrode/spiro-OMeTAD [58] and c-TiO₂/perovskite interfaces [59]. In addition, the incorporation of CQDs with ZnCl₂ (0.05:1% respectively) shows a significant increase in J_{sc} to about 23.5 mA/cm² with a low saturation current as shown in Fig. 7b. This suppresses charge carrier recombination and enhances shunt resistance and consequently achieves PCE of 8.08%.

4 Conclusion

Zn²⁺ ions were incorporated into the perovskite structure as a substitutional dopant to Pb²⁺. CQDs passivated the trap states on perovskite films and enlarged the grain size. The introduction of Zn²⁺ in perovskites yielded a compact, denser and pinholes free film with a larger grain size. In addition, the incorporation of CQDs produced a remarkable enhancement in grain size with negligible surface defects and an improvement in the crystallinity. ZnCl₂ (1%)/0.05 mg/mL CQDs perovskite film illustrated uniform grains distribution, high surface coverage with negligible pinholes and a larger grain size of 1.8 μm. By optimizing the ZnCl₂ and CQDs incorporation concentration, the device exhibited

PCE of 7.61 and 8.08% for FTO/c-TiO₂/1% ZnCl₂ doped perovskite/carbon electrode, and FTO/c-TiO₂/1% ZnCl₂/0.05 mg mL⁻¹ CQDs perovskite/carbon electrode, respectively.

Author contributions

All authors contributed to this work, conception and design. Material preparation, measurements and analysis were performed by HH, MS and SE. The first draft of the manuscript was written by HH and ZG. MSH has helped in the final modifications in the revised paper. All authors read and approved the final manuscript.

Funding

Open access funding provided by The Science, Technology & Innovation Funding Authority (STDF) in cooperation with The Egyptian Knowledge Bank (EKB). The authors did not receive support from any organization for the submitted work.

Data availability

The datasets generated during and/or analyzed during the current study are available from the first author upon reasonable request. Data sharing and data citation is encouraged.

Declarations

Competing Interests The authors have no conflict of interest to declare that are relevant to the content of this article.

Open Access This article is licensed under a Creative Commons Attribution 4.0 International License, which permits use, sharing, adaptation, distribution and reproduction in any medium or format, as long as you give appropriate credit to the original author(s) and the source, provide a link to the Creative Commons licence, and indicate if changes were made. The images or other third party material in this article are included in the article's Creative Commons licence, unless indicated otherwise in a credit line to the material. If material is not included in the article's Creative Commons licence and your intended use is not permitted by statutory regulation or exceeds the permitted use, you will need to obtain permission directly from the copyright holder. To view a copy of this licence, visit <http://creativecommons.org/licenses/by/4.0/>.

References

- B.J. Kim, H.S. Jung, in *Organic–Inorganic Halide Perovskite Photovoltaics: From Fundamentals to Device Architectures*, ed. by N.-G. Park, M. Grätzel, T. Miyasaka (Springer, Cham, 2016), pp. 3–5
- N.-G. Park, *Mater. Today* **18**, 65–72 (2015)
- R. Wang, M. Mujahid, Y. Duan, Z.K. Wang, J. Xue, Y. Yang, *Adv. Funct. Mater.* **29**, 1808843 (2019)
- J. Wang, G. Jin, Q. Zhen, C. He, Y. Duan, *Adv. Mater. Interfaces* **8**, 2002078 (2021)
- F. Gao, Y. Zhao, X. Zhang, J. You, *Adv. Energy Mater.* **10**, 1902650 (2020)
- M.M. Byranvand, M. Saliba, *Solar RRL* **5**, 2100295 (2021)
- A. Kausar, A. Sattar, C. Xu, S. Zhang, Z. Kang, Y. Zhang, *Chem. Soc. Rev.* **50**, 2696–2736 (2021)
- M. Pazoki, T. Edvinsson, *Sustain. Energy Fuels* **2**, 1430–1445 (2018)
- W. Zhao, Z. Yao, F. Yu, D. Yang, S. Liu, *Adv. Sci.* **5**, 1700131 (2018)
- J.T.-W. Wang, Z. Wang, S. Pathak, W. Zhang, D.W. deQuilletes, F. Wisnivesky-Rocca-Rivarola, J. Huang, P.K. Nayak, J.B. Patel, H.A.M. Yusof, *Energy Environ. Sci.* **9**, 2892–2901 (2016)
- L.A. Muscarella, D. Petrova, R.J. Cervasio, A. Farawar, O. Lugier, C. McLure, M.J. Slaman, J. Wang, E. von Hauff, R.M. Williams, *ACS Appl. Mater. Interfaces* **9**, 1678 (2017)
- T. Dudev, C. Lim, *J. Chin. Chem. Soc.* **50**, 1093–1102 (2003)
- G. Kieslich, S. Sun, A.K. Cheetham, *Chem. Sci.* **5**, 4712–4715 (2014)
- C. Li, X. Lu, W. Ding, L. Feng, Y. Gao, Z. Guo, *Acta Crystallogr. Sect. B: Struct. Sci.* **64**, 702–707 (2008)
- M.A. Green, A. Ho-Baillie, H.J. Snaith, *Nat. Photonics* **8**, 506–514 (2014)
- N.K. Noel, A. Abate, S.D. Stranks, E.S. Parrott, V.M. Burlakov, A. Goriely, H.J. Snaith, *ACS Nano* **8**, 9815–9821 (2014)
- L. Fagiolari, F. Bella, *Energy Environ. Sci.* **12**, 3437–3472 (2019)
- S. Ebrahim, M. Soliman, M. Anas, M. Hafez, T.M. Abdel-Fattah, *Int. J. Photoenergy* **2013**, 1–6 (2013)
- T.M. Abdel-Fattah, S. Ebrahim, M. Soliman, M. Hafez, *ECS J. Solid State Sci. Technol.* **2**, M13–M16 (2013)
- S.Y. Lim, W. Shen, Z. Gao, *Chem. Soc. Rev.* **44**, 362–381 (2015)
- H. Peng, Y. Li, C. Jiang, C. Luo, R. Qi, R. Huang, C.-G. Duan, *J. Travas-Sejdic Carbon* **100**, 386–394 (2016)
- A. Salem, S. El-Sheikh, F.A. Harraz, S. Ebrahim, M. Soliman, H. Hafez, I. Ibrahim, M. Abdel-Mottaleb, *Appl. Surf. Sci.* **425**, 156–163 (2017)
- Q. Guo, F. Yuan, B. Zhang, S. Zhou, J. Zhang, Y. Bai, L. Fan, T. Hayat, A. Alsaedi, Z. Tan, *Nanoscale* **11**, 115–124 (2018)
- Y. Ma, H. Zhang, Y. Zhang, R. Hu, M. Jiang, R. Zhang, H. Lv, J. Tian, L. Chu, J. Zhang, Q. Xue, H.L. Yip, R. Xia, X. Li, W. Huang, *ACS Appl. Mater. Interfaces* **11**, 3044–3052 (2019)
- H. Hou, C.E. Banks, M. Jing, Y. Zhang, X. Ji, *Adv. Mater.* **27**, 7861–7866 (2015)
- X. Wang, Y. Fang, L. He, Q. Wang, T. Wu, *Mater. Sci. Semicond. Process.* **27**, 569–576 (2014)
- P. Kartikay, A. Yella, S. Mallick, *Mater. Chem. Phys.* **256**, 123594 (2020)
- J. Jin, H. Li, C. Chen, B. Zhang, L. Xu, B. Dong, H. Song, Q. Dai, *ACS Appl. Mater. Interfaces* **9**, 42875–42882 (2017)
- N.J. Jeon, J.H. Noh, Y.C. Kim, W.S. Yang, S. Ryu, S.I. Seok, *Nat. Mater.* **13**, 897–903 (2014)
- M. Konstantakou, D. Perganti, P. Falaras, T. Stergiopoulos, *Crystals* **7**, 291 (2017)
- F. Du, F. Zeng, Y. Ming, S. Wu, *Microchim. Acta* **180**, 453–460 (2013)
- S. Zhu, Q. Meng, L. Wang, J. Zhang, Y. Song, H. Jin, K. Zhang, H. Sun, H. Wang, B. Yang, *Angew Chem.* **125**, 4045–4049 (2013)
- A. Sharma, T. Gadly, A. Gupta, A. Ballal, S.K. Ghosh, M. Kumbhakar, *J. Phys. Chem. Lett.* **7**, 3695–3702 (2016)
- C. Liu, P. Zhang, X. Zhai, F. Tian, W. Li, J. Yang, Y. Liu, H. Wang, W. Wang, W. Liu, *Biomaterials* **33**, 3604–3613 (2012)
- X. Gao, C. Du, Z. Zhuang, W. Chen, *J. Mater. Chem. C* **4**, 6927–6945 (2016)

36. X. Xing, L. Huang, S. Zhao, J. Xiao, M. Lan, *Microchem J.* **157**, 105065 (2020)
37. X. Sun, J. He, Y. Meng, L. Zhang, S. Zhang, X. Ma, S. Dey, J. Zhao, Y. Lei, *J. Mater. Chem. A* **4**, 4161–4171 (2016)
38. B. Kong, A. Zhu, C. Ding, X. Zhao, B. Li, Y. Tian, *Adv. Mater.* **24**, 5844–5848 (2012)
39. S. Mathew, A.R. Chacko, B.K. Korah, M.S. Punnose, B. Mathew, *Appl. Surf. Sci.* **606**, 154975 (2022)
40. M. Karim, A. Shokry, S. Ebrahim, M. Khalil, *Colloids Surf. Physicochem Eng. Aspects.* **652**, 129735 (2022)
41. B. Pakhira, M. Ghosh, A. Allam, S. Sarkar, *RSC Adv.* **6**, 29779–29782 (2016)
42. I.-M. Low, H.M. Albetran, M. Degiorgio, *J. Nanotechnol. Nanomaterials.* **1**, 23–30 (2020)
43. A. Bishnoi, S. Kumar, N. Joshi, in *Wide-angle X-ray diffraction (WXRD): technique for characterization of nanomaterials and polymer nanocomposites, in microscopy methods in nanomaterials characterization.* (Elsevier, Amsterdam, 2017), pp.313–337
44. P. Scherrer, *Nachr. Ges. Wiss Göttingen.* **26**, 98–100 (1918)
45. J.I. Langford, A. Wilson, *J. Appl. Crystallogr.* **11**, 102–113 (1978)
46. Hidayah, N., Liu, W.-W., Lai, C.-W., Noriman, N., Khe, C.-S., Hashim, U., Lee, H.C.: Comparison on graphite, graphene oxide and reduced graphene oxide: Synthesis and characterization, *AIP Conf. Proc.*, vol 1892, AIP Publishing LLC, 2017, p. 150002
47. R. Siburian, C. Simanjuntak, M. Supeno, S. Lumbanraja, H. Sihotang, *Orient. J. Chem* **34**, 182–187 (2018)
48. E. Aliyev, V. Filiz, M.M. Khan, Y.J. Lee, C. Abetz, V. Abetz, *Nanomaterials.* **9**, 1180 (2019)
49. W. Zhang, S. Pathak, N. Sakai, T. Stergiopoulos, P.K. Nayak, N.K. Noel, A.A. Haghghirad, V.M. Burlakov, D.W. DeQuillettes, A. Sadhanala, *Nat. Commun.* **6**, 1–9 (2015)
50. H. Zheng, G. Liu, X. Xu, A. Alsaedi, T. Hayat, X. Pan, S. Dai, *ChemSusChem* **11**, 3269–3275 (2018)
51. R. Chen, D. Hou, C. Lu, J. Zhang, P. Liu, H. Tian, Z. Zeng, Q. Xiong, Z. Hu, Y. Zhu, L. Han, *Sustain. Energy Fuels* **2**, 1093–1100 (2018)
52. Y. Wang, J. Zhang, S. Chen, H. Zhang, L. Li, Z. Fu, *J. Mater. Sci.* **53**, 9180–9190 (2018)
53. Q. Wei, J. Yin, O.M. Bakr, Z. Wang, C. Wang, O.F. Mohammed, M. Li, G. Xing, *Angew. Chem. Int. Ed.* **60**, 10957–10963 (2021)
54. F. Xu, T. Zhang, G. Li, Y. Zhao, *ChemSusChem* **10**, 2365–2369 (2017)
55. W. Zhao, D. Yang, Z. Yang, S. Liu, *Mater. Today Energy.* **5**, 205–213 (2017)
56. S. Guler, M. Unal, *Microsc. Res. Tech.* **81**, 1422–1433 (2018)
57. S. Zouhair, B. Luo, D. Bogachuk, D. Martineau, L. Wagner, A. Chahboun, S.W. Glunz, A. Hinsch, *Sol. RRL.* **6**, 2100745 (2022)
58. H. Chen, Z. Wei, H. He, X. Zheng, K.S. Wong, S. Yang, *Adv. Energy Mater.* **6**, 1502087 (2016)
59. X. Wu, L. Xie, K. Lin, J. Lu, K. Wang, W. Feng, B. Fan, P. Yin, Z. Wei, *J. Mater. Chem. A* **7**, 12236–12243 (2019)

Publisher's Note Springer Nature remains neutral with regard to jurisdictional claims in published maps and institutional affiliations.